

Showcasing research from Professor Wei Wang's laboratory, Department of Mechanical Engineering, Hanyang University, Seoul, Korea.

Robotic soft swim bladder using liquid-vapor phase transition

An entire soft swim bladder based on the liquid-vapor phase transition has been developed, which can selectively and noiselessly control buoyancy, thereby allowing multiple modes of manoeuvres for underwater robots. This work opens up a new avenue for depth control mechanisms for underwater biomimetic applications that benefit from soft materials.

As featured in:



See Wei David Wang *et al.*,
Mater. Horiz., 2021, **8**, 939.



Robotic soft swim bladder using liquid–vapor phase transition†

Beomchan Kang, Yongkyu Lee, Tailin Piao, Zhengbing Ding and Wei David Wang *

Cite this: *Mater. Horiz.*, 2021, **8**, 939

Received 6th November 2020,
Accepted 13th January 2021

DOI: 10.1039/d0mh01788d

rsc.li/materials-horizons

The swim bladder is crucial to underwater robots to enhance their overall performance and to expand their range of motion. However, previous attempts to incorporate this function have failed or have adopted mechanical swim bladders with high-disturbances. This study presents an entirely soft swim bladder capable of controlling buoyancy selectively and noiselessly, making it applicable to sensitive underwater environments. The soft swim bladder, which consists of an elastic cover layer, flexible heating elements, and three expandable pouches filled with low boiling point fluid, can express four modes of motion by varying buoyancy: sinking, suspending, rising, and fast-rising. The varying buoyancy is achieved through liquid–vapor phase transition of the fluid in the selected pouches when Joule heated above its boiling temperature. Moreover, the swim bladder is integrated with a shape memory alloy-based fishtail to form a soft fish robot. The synergy between the bladder and the tail allows the robot to explore a total of ten disparate modes of maneuvers, and their dynamic performance has been evaluated. The results of this study present the potential for the soft swim bladder to be utilized in any underwater robotic applications to enhance their swimming performance.

Introduction

Marine environments have been of great interest to many researchers due to their biodiversity and rich resources.^{1,2} This growing interest has led to a demand for versatile underwater robots that are capable of carrying out a wide range of duties,^{3–5} particularly observation. As a consequence, remotely operated vehicles and autonomous underwater vehicles were developed to swim alongside wildlife^{4,6} to accomplish advanced underwater observation. These robots, however, are typically built by assemblies of rigid components such as motors, pumps, and gears,⁷ displaying an overall foreign look that prevents

Department of Mechanical Engineering, Hanyang University, Seoul 04763, South Korea. E-mail: davidwang@hanyang.ac.kr, hitwangw@hotmail.com

† Electronic supplementary information (ESI) available. See DOI: 10.1039/d0mh01788d

New concepts

We pioneer the use of the principle of liquid–vapor phase transition to design a depth control mechanism for underwater robotic applications. The function of the mechanism is achieved through volume change from Joule heating-induced phase transition of the low boiling point fluid inside the buoyancy pouch. Like the swim bladder found in bony fish which allows efficient depth control, the equivalent is necessary for underwater robots to add diversity to their range of motion. While previous studies incorporated this function through assemblies of complex rigid components that require large space and peripherals, our proposed method is based on a simple principle that consists entirely of soft materials. This study highlights the effective control of depth demonstrated through a soft fish robot. The result of this work opens a new avenue for a simple depth control mechanism in underwater biomimetic applications that benefit from soft materials.

capturing marine life in their most natural behavior. The bulk and high-noise properties of rigid robots are likely to disturb the surroundings, thereby limiting their use in sensitive environments. Since close-up observation requires more low-profile and low-disturbance characteristics, a generation of soft robots using biomimicry has surfaced. These alternative soft robots are mainly actuated with the use of smart materials,^{8–15} which enables a smooth, continuous motion that accurately mimics real-life animals. This feature allows for better blending of the robot to its environment, giving rise to an upgraded level of observation at a new angle that cannot be achieved using traditional rigid robots.

Previous underwater exploration robots have utilized various methods such as jumping,¹⁶ walking,^{17,18} jetting,^{19,20} and swimming^{21–23} to achieve motion underwater. These robots, however, are confined to functioning only at a specified depth such as the seabed, mid-water, or water surface and are unable to control their depth in water. Considering the unpredictable nature of the marine habitat, robots with depth controlling mechanisms have an edge in adapting to such environments.^{5,24–27} For some robots that require a rigorous temperature range to function properly, depth control is mandatory for location at the right depth and temperature. Besides, complicated geographical

features that include underwater tunnels, water ice, valleys, and coral reefs also reinforce the need for a depth control system for a robot to avoid these obstacles precisely and safely.^{5,28,29}

These compelling reasons for the need for such a mechanism have led to the development of underwater robots that can control their vertical location. However, many previous mechanisms have limitations that restrict their use in certain situations. For example, underwater fish robots that utilize pectoral fins to generate upward-lifting force in water require extra space and cannot function suitably in tight surroundings.^{30–33} Besides, controlling the gas level to adjust the buoyancy requires the use of gas pumps^{7,34,35} and complex mechanical elements³⁶ such as a hydraulic cylinder, motor, and valve, which result in a complex and tedious fabrication process as well as noise disturbances in the environment.^{37–40} The use of external structures such as fins and wings entails other components that add size to the overall system,^{30,33,41} causing limitations on applications in an obstacle-filled underwater environment. In addition, the use of rigid components in the previously mentioned studies makes them unsuitable for biomimetic soft robotic applications.^{9,42} In contrast, the buoyancy control system based on liquid–vapor phase transition materials proposed in this work is eco-friendly and consists entirely of soft structures, which

therefore can serve as a solution to problems found in prior studies.

In this study, a bioinspired soft swim bladder for underwater applications was proposed using liquid–vapor phase transition capable of selectively varying buoyancy force. This function enables underwater robots to express different modes of motion including sinking, suspending, and rising. Using a material that can easily change phase between liquid and vapor by Joule heating or cooling enables the soft swim bladder to exhibit various states such as positive, neutral, and negative buoyancy. A soft swim bladder was fabricated consisting of three buoyancy pouches filled with low boiling point fluid, flexible heating elements, and an elastic cover layer. Its dynamic properties were analyzed based on the number of working buoyancy pouches. As a demonstration, the bladder was integrated with a shape memory alloy (SMA)-based fishtail to construct a soft fish robot, and the synergy between the bladder and the tail enables a total of ten disparate modes of maneuvers of the fish robot. The dynamic performance of the fish robot was then evaluated, which included swimming forward, vertically, and diagonally under different actuation patterns. This study demonstrates the use of an inflatable soft swim bladder to adjust the buoyancy force to control the depth

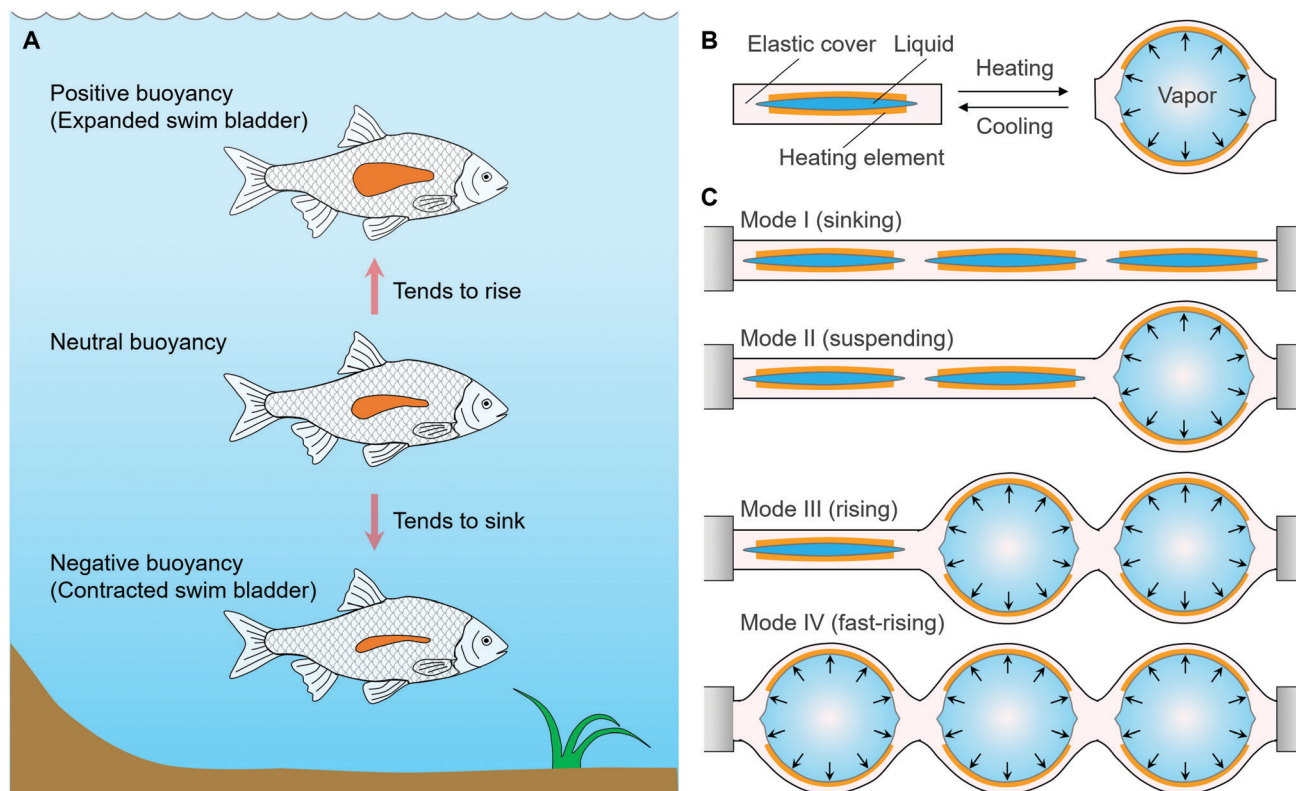


Fig. 1 Working principle and concept design of the soft swim bladder. (A) A fish can adjust its depth in water by controlling and changing the volume of the swim bladder to generate positive, neutral, and negative buoyancy for rising, suspending, and sinking, respectively. (B) Schematic of the pouch filled with low boiling point fluid capable of expanding its volume *via* phase transition of the fluid from liquid to vapor when Joule heated above its boiling temperature. The pouch contracts to its original state through rapid free cooling in water. (C) Four different configurations of the soft swim bladder (mode I sinking, mode II suspending, mode III rising, and mode IV fast-rising), consisting of three pouches that can be actuated separately.

of an underwater robot without the requirement of complex and rigid mechanical elements.

Results and discussion

Many bony fish can freely control depth in water using their swim bladder, an internal gas-filled organ that can adjust the amount of gas within,^{43,44} as seen in Fig. 1A. This function allows a fish to maintain its position in a neutral buoyancy state when its average density is equivalent to the water density. Furthermore, negative or positive buoyancy causes the body to sink or rise when the body density becomes greater or lower than that of water, once the swim bladder is contracted or expanded. To mimic the function of this biological organ, the robotic soft swim bladder proposed in this work operates on liquid–vapor phase transition principles in inflatable buoyancy pouches to control the buoyant force. The inflatable buoyancy pouch was filled with a phase transition material (engineered fluid with a low boiling point), which rapidly expands when heated above its boiling point through the embedded flexible heating elements (Fig. 1B). Conversely, when a buoyancy pouch filled with vapor is free cooled to the liquid state below its boiling point, it quickly contracts. The two reversible processes are used to control buoyancy by altering density in a sealed soft pouch due to the change in volume while maintaining the same weight. Two states of the pouch are used in this study, that is, a fully expanded state with maximum deformation and a fully contracted state without deformation; their intermediate state is not considered. The soft swim bladder is designed with three identical buoyancy pouches for generating different buoyant forces, as shown in Fig. 1C. The three identical pouches in the swim bladder allow the configuration of four modes: sinking, suspending, rising, and fast-rising, depending on the number of working pouches.

The fabrication process of the proposed soft swim bladder is described in Fig. 2A. The process mainly includes the following

steps: heat-sealing of the thin films, injection of the engineered fluid, and assembly of the swim bladder with all other functional components including flexible heating elements and the polymer-based elastic cover. Thermoplastic polyurethane (TPU) was chosen as the material for the thin sealable film mainly due to its rapid heat transfer from the heating element, high-temperature resistance, and relatively low permeability coefficient. The engineered fluid with a boiling point of 49 °C was chosen as the phase-transition material for two main reasons. The first is its significant volume change by two orders of magnitude, and the next reason is its low boiling temperature compared to that of water, which also falls well within the working temperature range of TPU. The main properties of the engineered fluid are summarized in Table S1 (ESI†). Elastic covers were used to properly adjust the heat transfer between the pouch set and the surrounding water. The detailed fabrication process is described in the ESI.† The schematics of the cross-sections of the fabricated soft swim bladder before and after full expansion are described in Fig. 2B.

The first step was to evaluate the effect of the dimensions of one buoyancy pouch on its maximum expansion deformation. To do so, the length of the pouch was fixed at 30 mm and the width was varied from 5 mm to 15 mm in 1 mm increments (the upper inset of Fig. 3A). The maximum expansion deformation perpendicular to the sealing plane was measured for each pouch after immersing the pouch in hot water of 60 °C for instant expansion. Both the experimental and modeling results are illustrated (Fig. 3A and Fig. S1, ESI†). One can see that the relationship between the maximum expansion deformation of the pouch and the pouch width is approximately linear. Besides, to investigate the effect of external pressure on pouch expansion, that is, to find the operating depth range of the proposed mechanism, the maximum expansion deformation of the buoyancy pouch was tested under different pressure conditions (Fig. 3B). Results show that the maximum deformation rapidly decreased as the applied pressure was increased. Hence, the operating depth of the buoyancy pouch with less

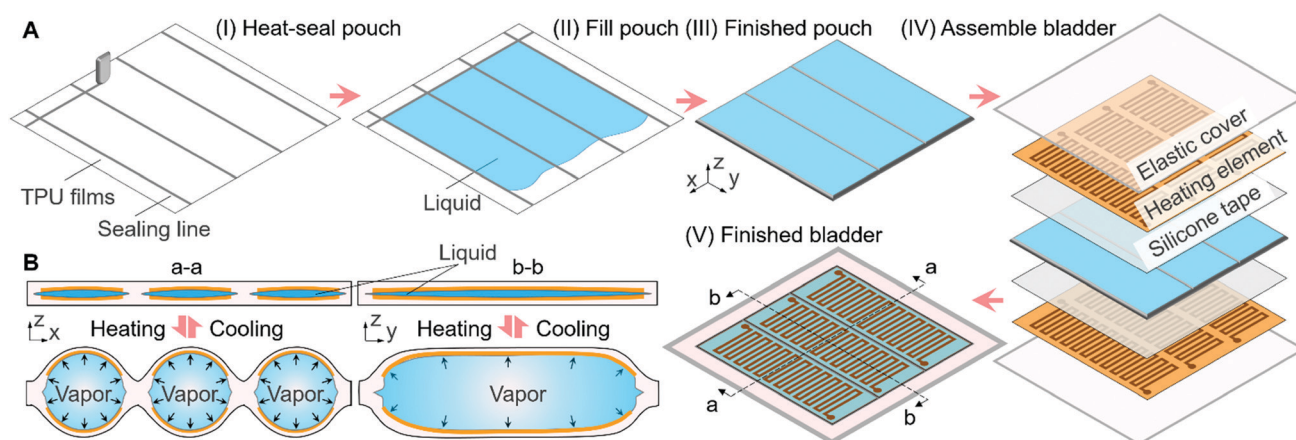


Fig. 2 Fabrication process of the soft swim bladder. (A) Two TPU films are first sealed using an impulse sealer, leaving one side open for injecting fluid. Each pouch is then filled with a certain volume of liquid–vapor convertible fluid, and all pouches are sealed. After preparing the complete pouches, the flexible heating elements are pasted to both surfaces of the pouch set using double-sided silicone tape. Finally, the assembly is covered with a thin elastic cover. (B) Schematics of the cross-section of the fabricated swim bladder composed of three pouches before and after actuation.

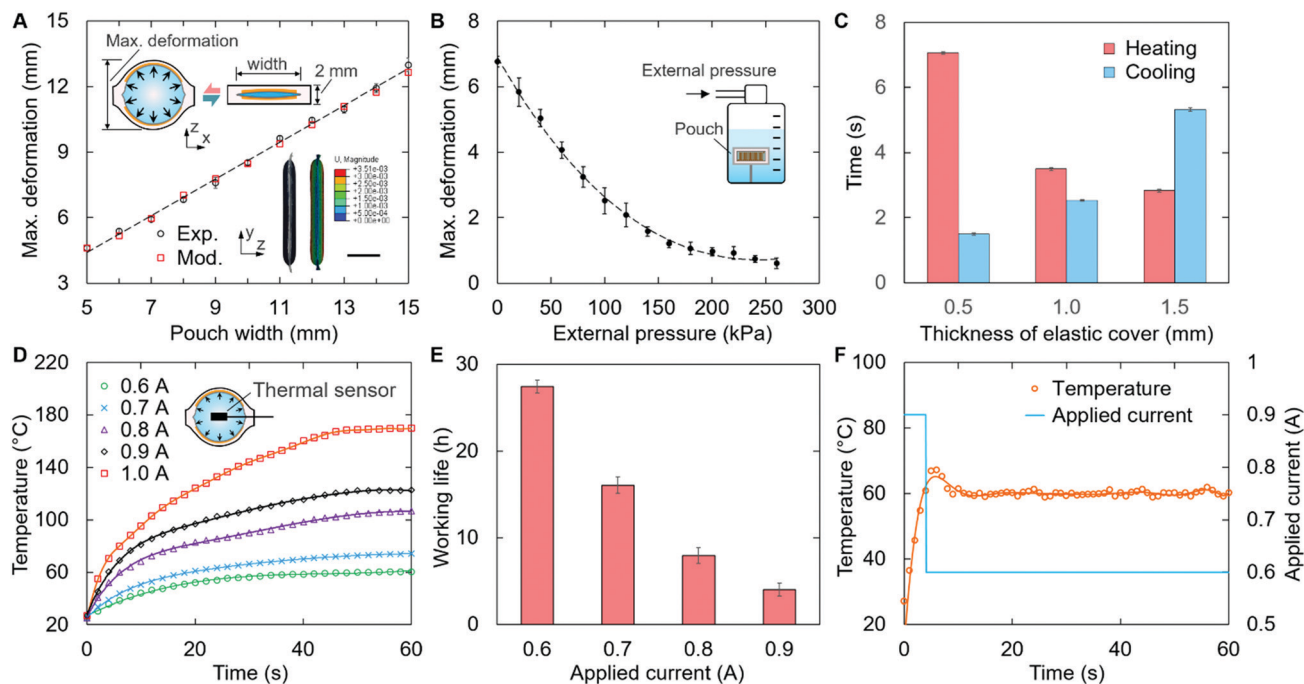


Fig. 3 Optimization of the buoyancy pouch that includes an elastic cover and heating elements. (A) Comparison of the experimental and modeling results for maximum expansion deformation for different pouch widths. The upper inset shows the schematic of the buoyancy pouch with its main dimensions and the bottom inset shows the experimental and modeling results for a fully inflated pouch with a width of 8 mm. The scale bar is 10 mm. (B) The expansion deformation of the pouch with a fixed dimension of 8 mm in width and 30 mm in length for varied applied external pressure. The inset shows the schematic of the experimental setup. (C) Heating and cooling times required to achieve maximum inflated deformation of the buoyancy pouch with different thicknesses of the elastic cover in the water at 21 °C. (D) The internal temperature of the pouch changes with time under different currents. The temperature was measured using an embedded thermal sensor as shown in the inset. (E) Working time of the pouch when different currents are continuously applied. (F) Customized current pattern to maintain the maximum inflated deformation of the pouch by keeping the internal temperature at 60 °C. The input current of 0.9 A was applied for 3 s, followed by the drop in current to 0.6 A.

influence of pressure is defined in this study to be within 5 m (*i.e.*, corresponding to 50 kPa) which is the depth of relatively shallow waters like rivers and lakes.

The heating and cooling times required to expand or contract the buoyancy pouch depend on the rate of heat transfer through the elastic cover, which is mainly determined by its thickness. For a quantitative measure, the cooling and heating times with elastic covers of thicknesses 0.5 mm, 1 mm, and 1.5 mm were measured in water of 21 °C when an electrical current of 0.8 A was applied to the heating elements. If not specified, all the follow-up experiments performed in water in this study were conducted at the same water temperature. Fig. 3C shows the times required to achieve maximum inflated deformation and restoration to the original state through free cooling for different values of thickness. The results show that longer heating and cooling times were required for greater thickness since the lower heat-transfer rate slows down heat dissipation to ambient water. To achieve both a rapid heating and cooling time, the thickness of 1 mm was selected, resulting in a heating rate of 2.5 s and a cooling rate of 3.5 s.

To optimize the current applied to heat the fluid *via* Joule heating, the internal temperatures of the identical samples were measured for 60 s. The recorded peak temperatures were 60, 74, 106, 122, and 169 °C for 0.6, 0.7, 0.8, 0.9, and 1.0 A, respectively (Fig. 3D). The calculated working life as a function of the applied current shows a marked decrease, recording

approximately 27 h for 0.6 A, 16 h for 0.7 A, 8 h for 0.8 A, and 4 h for 0.9 A (Fig. 3E). It is worth noting that the peak temperature at 0.9 A was nearly 120 °C, which is close to the theoretical heat distortion temperature of the TPU. Continuous heat application at this current resulted in quick failure of the pouch.

Hence, to enhance the working life of the pouches, the current intensity was weakened once the maximum deformation was reached, to prevent prolonged heating at extreme temperatures. Consequently, a customized current signal was designed to actuate each pouch rapidly and safely to its full deformation. This approach was accomplished by first applying 0.9 A for 3 s to inflate the pouch rapidly, followed by a drop in current to 0.6 A to maintain the fully inflated deformation by keeping the internal temperature at around 60 °C. Fig. 3F presents the temperature change rate for the applied customized current signal during the continuous operation of the pouches. It is worth noting that continuous application of current is not required to drive the soft swim bladder when adjusting the depth underwater. Even for the suspending mode, which is achieved through the expanded state of a single pouch, it is not necessary to continuously actuate one buoyancy pouch exclusively. Rather, the methodology of alternately actuating the three pouches after a certain period prevents any pouch from extended heat exposure that degrades the working life. Additional experiments were conducted with a customized current cycle that included cooling to calculate a more practical working

life, and the results show that the working life was increased by several times (Fig. S2, ESI†).

The working life of the pouch is also affected by the permeability of the TPU film. To examine the degree of penetration of the engineered fluid through the TPU at both phases, the changes in weight of the fluid-containing pouch were measured over time at two different temperatures of 21 °C and 60 °C (Fig. S3, ESI†). The results illustrate that the weight change was negligible when the engineered fluid was maintained at the liquid phase at 21 °C. On the other hand, the weight of the expanded pouch above the boiling point at 60 °C showed a steady decline over time, preserving approximately 85% of the initial weight after around 70 h. However, applying continuous heat for an extended period is a highly unlikely scenario, since the operation of the swim bladders will consist of current cycles with intermittent cooling periods, which keeps the fluid in the liquid phase. Besides, to compensate for the loss at high temperatures, the amount of the fluid filled in the pouch is much larger than the amount of fluid required for the maximum expansion. Therefore, the effects of fluid loss through penetration in the soft swim bladder are only minimal.

The robotic soft swim bladder consists of three buoyancy pouches with overall dimensions of 40 × 50 × 2 mm (width × length × thickness) with a weight of about 5 g (Fig. S4, ESI†). The swim bladder can express four different configurations, including one initial state and three different inflated states including one, two, and three inflated pouches, corresponding to the four different modes of motion (Fig. 1C and 4A). The three inflated configurations were achieved by selectively Joule heating one, two, and three pouches, respectively, and the buoyancy forces were measured for each of the configurations. The experimental setup is illustrated in the inset of Fig. 4B, in which the swim bladder was fixed to a load cell using a cable through a pulley that can freely rise vertically corresponding to the generated buoyancy. An adjustable float was attached to the swim bladder to counteract its gravity so that the initial buoyancy is zero without any inflated pouches. To measure the maximum buoyancy at their fully expanded states, the current of 0.9 A was applied for 5 s. The relationship between the maximum buoyancy of the swim bladder and the number of working pouches was approximately linear, as the measured values were around 12.5 mN, 24.5 mN, and 36.4 mN for one, two, and three working pouches (Fig. 4B).

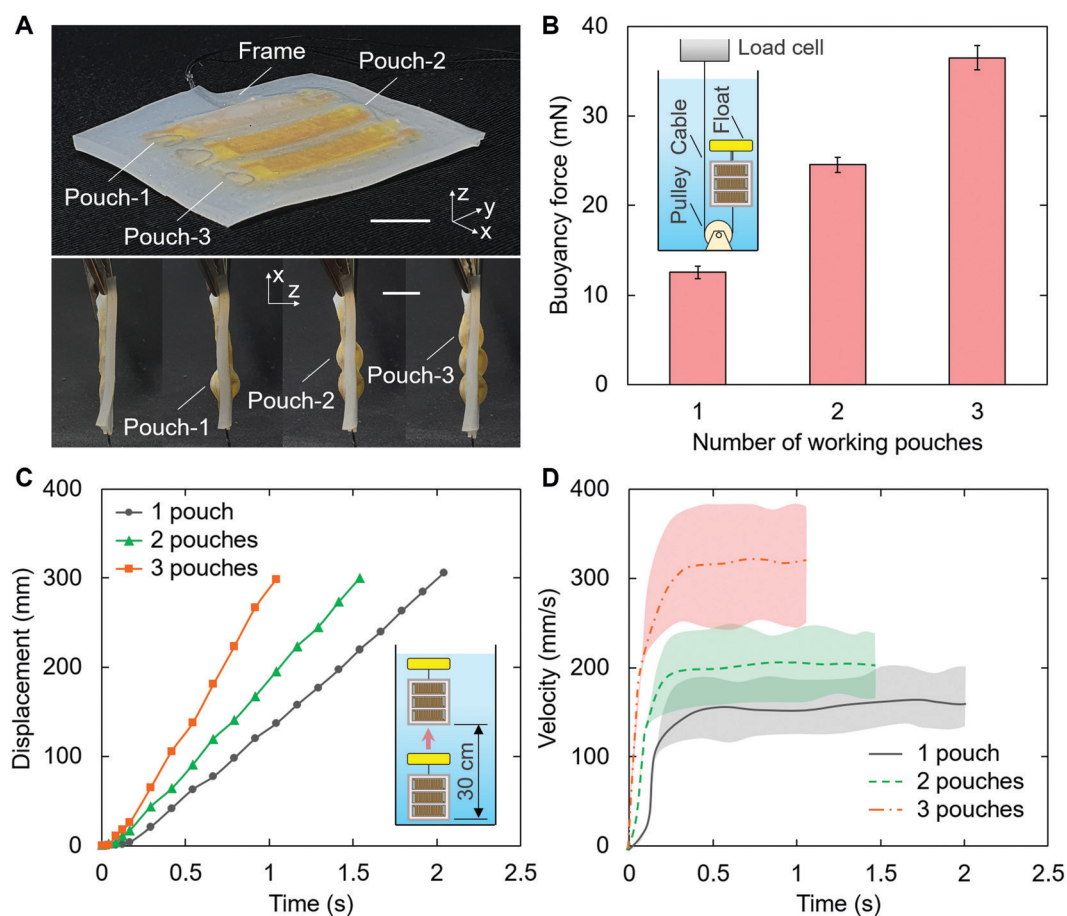


Fig. 4 Dynamic performance of the soft swim bladder. (A) Fabricated swim bladder consisting of three buoyancy pouches capable of obtaining four different configurations, one initial state and three inflated states with one, two, and three inflated pouches. All scale bars are 5 mm. (B) Measured buoyancy force of the swim bladder for different numbers of working pouches and an inset of the experimental setup. (C) Measured displacement–time curves for a swim bladder with one, two, and three working pouches at a fixed running distance of 30 cm and an inset of the experimental setup. (D) The experimental results for the instantaneous velocity of the swim bladder for different numbers of working pouches.

The behavioral properties of the swim bladder for rising or sinking were determined by the generated buoyant force. To further investigate the performance of the swim bladder, the instantaneous velocity was experimentally calculated for one, two, and three working pouches. All experiments were conducted in the water at a fixed running distance of 30 cm and the measured data were calculated based on frames from the

recorded video, as illustrated in the inset of Fig. 4C. The measured displacement–time curves are shown in Fig. 4C. The elapsed time for one, two, and three working pouches was around 1.1 s, 1.6 s, and 2.1 s, respectively. The experimental instantaneous velocities are illustrated in Fig. 4D. Results show that the instantaneous velocity for all cases rapidly increases at first, and then converges

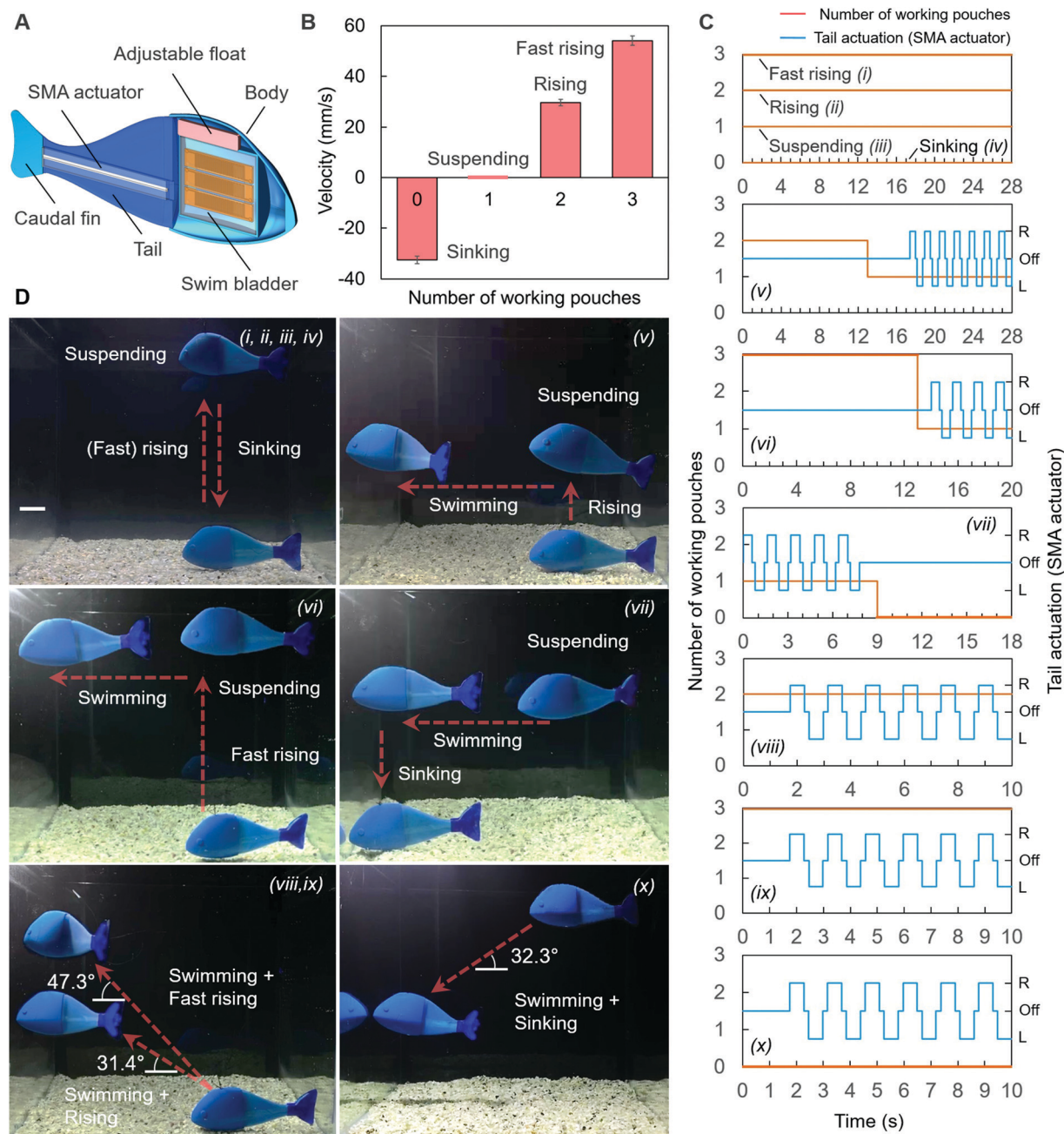


Fig. 5 Performance of the soft fish robot. (A) Schematic of the cross-section of the fish robot indicating its main components and their relative positions. (B) Measured terminal velocities of four different modes of vertical motions of the fish robot in the water: sinking, suspending, rising, and fast-rising using zero, one, two, and three working pouches, respectively. (C) Actuation patterns of the swim bladder and fishtail for a total of ten disparate modes of maneuvers of the fish robot (D) as follows: (i) rising, (ii) fast-rising, (iii) suspending, (iv) sinking, (v) rising-swimming, (vi) fast-rising-swimming, (vii) swimming-sinking, (viii) diagonal rising, (ix) diagonal fast-rising, and (x) diagonal sinking. The sub-figures with the same Roman numerals in (C) and (D) indicate that both are pairs. The scale bar is 30 mm.

to an approximately stable velocity (154.3 mm s⁻¹, 201.3 mm s⁻¹, and 319.5 mm s⁻¹, respectively), defined as the terminal velocity. This is because the buoyant force at the beginning is greater than the sum of the drag force exerted on the swim bladder and its weight, and then the gradual increase in the drag force enables an equilibrium to be achieved among these forces. It can be seen that there is a positive correlation between the terminal velocity and the number of working pouches. The findings of this experiment demonstrate that easy control of the depth is achieved by increasing or decreasing the number of working pouches to vary the buoyancy.

Here, the functionality of the robotic soft swim bladder was demonstrated through integration into an SMA-based soft fish robot mainly consisting of the head and tail parts (Fig. 5A and Fig. S5, ESI†). The fish head was designed with an inner cavity to accommodate the soft swim bladder and the adjustable floats. Through modulating the floats, the overall density of the robot was set to be slightly greater than that of water to maintain neutral buoyancy when a single pouch of the bladder was expanded. Consequently, such a modification of the overall density of the robot allowed us to depend solely on the effects of the swim bladder to control buoyancy for four different modes of motion (Fig. 1C). The fishtail was actuated by an SMA-based soft actuator containing two SMA wires that were alternately actuated to achieve a side-to-side thrust of the caudal fin to propel the fish robot forwards.^{8,45–48} Details on the fabrication and control of the fish robot are explained in the ESI.†

To assess the rising and sinking capability of the fish robot, its terminal velocities were measured for different numbers of working pouches of the swim bladder. The terminal rising velocities were measured at around 29.7 mm s⁻¹ and 54.1 mm s⁻¹ for two and three working pouches, respectively. Similarly, the sinking mode was triggered if all the pouches were unexpanded, at which the calculated terminal sinking velocity was around 32.5 mm s⁻¹ (Fig. 5B). The customized actuation pattern of the SMA-based caudal fin enabled the robot to achieve a forward swimming speed of approximately 28.8 mm s⁻¹, which is described in the ESI.† The effects of the swim bladder and the fishtail actuator were then combined with modifications of the actuation pattern, which enabled a total of ten disparate modes of maneuvers (Fig. 5C and D). The red and blue lines in the graphs in Fig. 5C indicate the number of actuated pouches and the tail actuation pattern, respectively. Each sub-number depicted in the Roman numerals in Fig. 5C and D relates the control sequence of each motion and the corresponding visualization.

Four different modes of vertical motions of the fish robot characterized as sinking, suspending, rising, and fast-rising were first obtained through the variation in the number of working pouches (Fig. 5C and D from (i) to (iv) and Movie S1, ESI†). The next two modes are rising-swimming and fast-rising-swimming achieved by first utilizing two and three working pouches, respectively, then maintaining at a single working pouch to achieve neutral buoyancy, followed by tail actuation to trigger forward movement (Fig. 5D(v), (vi) and Movie S2, ESI†). The next mode defined as swimming-sinking is illustrated in Fig. 5D(vii). In contrast to the prior modes, tail actuation was

executed while maintaining neutral buoyancy. Then, the swim bladder was un-actuated to enable the fish robot to achieve a sinking motion (Movie S3, ESI†). The remaining three modes incorporate diagonal movements including diagonal rising with two working pouches (Fig. 5D(viii) and Movie S4, ESI†), diagonal fast-rising with three working pouches (Fig. 5D(ix) and Movie S4, ESI†), and diagonal sinking with no working pouch (Fig. 5D(x) and Movie S5, ESI†). These movements were realized through simultaneous actuation of the swim bladder and the tail. It can be observed that the rising angle of the diagonal fast-rising movement is steeper than that of the diagonal rising movement, with the respective rising angle values being 47.3° and 31.4° for each case. Similarly, the calculated sinking angle was around 32.3° for the diagonal sinking movement.

Conclusions

This study developed a robotic soft swim bladder for underwater applications based on liquid–vapor phase transition capable of selective control of buoyancy. The swim bladder is composed entirely of soft materials, without the use of complex mechanical elements and rigid components. The swim bladder consists of three identical pouches whose expanded deformation can be independently triggered by Joule heating above its boiling temperature. These three pouches enable the swim bladder to alter its buoyancy to achieve four different configurations: sinking, suspending, rising, and fast-rising. After integrating the soft swim bladder into a soft fish robot, a total of ten disparate modes of maneuvers of the fish robot can be accomplished by combining the effects of the swim bladder and the actuation of the fishtail. This capability enables the fish robot to successfully maneuver in complex underwater environments.

Compared with other depth control mechanisms of underwater robots in previous studies, the soft swim bladder proposed in this study exhibits several promising qualities. First, the use of a soft inflatable mechanism based on liquid–vapor phase transition allows for a rapid volume expansion by two orders of magnitude during vaporization, resulting in a significant buoyancy change without using any complex components. Second, the proposed soft swim bladder is free from causing any noise and vibration disturbances to allow better blending of the robot to sensitive marine environments. Furthermore, the inherent softness together with the compact and lightweight configuration of the swim bladder permits easy integration into soft biomimetic robots. Besides, unlike fin-like mechanisms that require external space, the proposed soft swim bladder can be installed internally, which enables depth control in tight surroundings. At the same time, some challenges remain for the current design of the proposed mechanism, including working life issues concerning heat accumulation and film permeability. Also, for this study, the motion of the soft swim bladder was controlled in a wired manner due to difficulties associated with accommodating power source when establishing an untethered system. Future works include extending the working life of the soft swim bladder by applying different

triggering strategies and adopting a vapor-blocking layer or changing the cover material to mediate the vapor penetration issue. Lastly, we aim to develop a remote-controlled untethered robotic system with closed-loop control to monitor and optimize the pressure and generated heat to enhance performance.

Experimental section

Experimental procedures and additional data are available in the ESI.†

Author contribution

W. W. designed the study. B. K., T. P., Y. L., and Z. D. performed the experiments. B. K. and Y. L. analyzed the results. B. K., Y. L., and W. W. wrote the paper.

Conflicts of interest

There are no conflicts to declare.

Acknowledgements

This work was supported by the National Research Foundation of Korea (NRF) grant funded by the Korea government (MSIT) (No. 2020R1C1C1010295). The deepest gratitude is expressed to the Lord Jesus Christ. The authors would like to thank the reviewers for their insightful feedback.

References

- W. W. L. Cheung, T. L. Frolicher, R. G. Asch, M. C. Jones, M. L. Pinsky, G. Reygondeau, K. B. Rodgers, R. R. Rykaczewski, J. L. Sarmiento, C. Stock and J. R. Watson, *ICES J. Mar. Sci.*, 2016, **73**, 1283–1296.
- T. R. McClanahan, M. J. Marnane, J. E. Cinner and W. E. Kiene, *Curr. Biol.*, 2006, **16**, 1408–1413.
- J. Yuh, *IEEE Trans. Syst. Man Cybern.*, 1990, **20**, 1475–1483.
- I. C. Robbins, G. J. Kirkpatrick, S. M. Blackwell, J. Hillier, C. A. Knight and M. A. Moline, *Harmful Algae*, 2006, **5**, 749–761.
- J. G. Mooney and E. N. Johnson, *J. Intell. Robot. Syst.*, 2014, **33**, 1–17.
- R. Bogue, *Ind. Rob.*, 2015, **42**, 186–191.
- H. Xu, C. Pan, H. Xie and D. Zhang, *J. Bionic Eng.*, 2008, **5**, 66–71.
- Z. Wang, G. Hang, J. Li, Y. Wang and K. Xiao, *Sens. Actuators, A*, 2008, **144**, 354–360.
- T. Li, G. Li, Y. Liang, T. Cheng, J. Dai, X. Yang, B. Liu, Z. Zeng, Z. Huang, Y. Luo, T. Xie and W. Yang, *Sci. Adv.*, 2017, **3**, 1–8.
- D. Lei, Y. Yang, Z. Liu, S. Chen, B. Song, A. Shen, B. Yang, S. Li, Z. Yuan, Q. Qi, L. Sun, Y. Guo, H. Zuo, S. Huang, Q. Yang, X. Mo, C. He, B. Zhu, E. M. Jeffries, F. L. Qing, X. Ye, Q. Zhao and Z. You, *Mater. Horiz.*, 2019, **6**, 394–404.
- Z. Liu, Y. Wang, Y. Ren, G. Jin, C. Zhang, W. Chen and F. Yan, *Mater. Horiz.*, 2020, **7**, 919–927.
- M. Behl, M. Y. Razzaq and A. Lendlein, *Adv. Mater.*, 2010, **22**, 3388–3410.
- A. Villanueva, C. Smith and S. Priya, *Bioinspir. Biomim.*, 2011, **6**, 036004.
- N. Kellaris, V. Gopaluni Venkata, G. M. Smith, S. K. Mitchell and C. Keplinger, *Sci. Rob.*, 2018, **3**, eaar3276.
- S. Taccola, F. Greco, E. Sinibaldi, A. Mondini, B. Mazzolai and V. Mattoli, *Adv. Mater.*, 2015, **27**, 1668–1675.
- J. S. Koh, E. Yang, G. P. Jung, S. P. Jung, J. H. Son, S. I. Lee, P. G. Jablonski, R. J. Wood, H. Y. Kim and K. J. Cho, *Science*, 2015, **349**, 517–521.
- G. Picardi, M. Chellapurath, S. Iacoponi, S. Stefanni, C. Laschi and M. Calisti, *Sci. Rob.*, 2020, **1012**, 1–15.
- M. Ishida, D. Drotman, B. Shih, M. Hermes, M. Luhar and M. T. Tolley, *IEEE Rob. Autom. Lett.*, 2019, **4**, 4163–4169.
- R. Zufferey, A. Ortega Ancel, A. Farinha, R. Siddall, S. F. Armanini, M. Nasr, R. V. Brahmam, G. Kennedy and M. Kovac, *Sci. Rob.*, 2019, **4**, eaax7330.
- Y. Wang, S. Pang, H. Jin, M. Xu, S. Sun, W. Li and S. Zhang, *Bioinspir. Biomim.*, 2020, **15**, 036008.
- F. Shi, J. Niu, J. Liu, F. Liu, Z. Wang, X. Q. Feng and X. Zhang, *Adv. Mater.*, 2007, **19**, 2257–2261.
- B. Chen and H. Jiang, *Soft Robot.*, 2019, **6**, 520–531.
- J. Zhu, C. White, D. K. Wainwright, V. Di Santo, G. V. Lauder and H. Bart-Smith, *Sci. Rob.*, 2019, **4**, eaax4615.
- T. J. Webb, E. vanden Berghe and R. O'Dor, *PLoS One*, 2010, **5**, 1–6.
- B. H. Robison, *J. Exp. Mar. Biol. Ecol.*, 2004, **300**, 253–272.
- R. Kunzig, *Science*, 2003, **302**, 991.
- J. M. Roberts, A. J. Wheeler and A. Freiwald, *Science*, 2006, **312**, 543–547.
- H. Singh, T. Maksym, J. Wilkinson and G. Williams, *Sci. Rob.*, 2017, **2**, eaan4809.
- J. G. Bellingham and K. Rajan, *Science*, 2007, **318**, 1098–1102.
- S. R. Shin, B. Migliori, B. Miccoli, Y. C. Li, P. Mostafalu, J. Seo, S. Mandla, A. Enrico, S. Antona, R. Sabarish, T. Zheng, L. Pirrami, K. Zhang, Y. S. Zhang, K. tak Wan, D. Demarchi, M. R. Dokmeci and A. Khademhosseini, *Adv. Mater.*, 2018, 1704189.
- A. Raj and A. Thakur, *Bioinspir. Biomim.*, 2016, **11**, 031001.
- K. H. Low, *Proc. Inst. Mech. Eng. Part I J. Syst. Control Eng.*, 2007, **221**, 295–309.
- R. K. Katzschnmann, J. DelPreto, R. MacCurdy and D. Rus, *Sci. Rob.*, 2018, **3**, eaar3449.
- J. Wang, H. Zhang, Y. Wang, Y. Liu, Z. Wu, Y. Liang and M. Yang, *Ocean. 2017 - Aberdeen*, 2017, 2017–October, 1–5.
- S. Tangirala and J. Dzielski, *IEEE J. Ocean. Eng.*, 2007, **32**, 762–771.
- M. Ikeda, S. Hikasa, K. Watanabe and I. Nagai, *Artif. Life Rob.*, 2014, **19**, 136–141.
- D. Ross, *IEEE J. Ocean. Eng.*, 2005, **30**, 257–261.
- M. F. McKenna, D. Ross, S. M. Wiggins and J. A. Hildebrand, *J. Acoust. Soc. Am.*, 2012, **131**, 92–103.

- 39 P. T. Madsen, M. Wahlberg, J. Tougaard, K. Lucke and P. Tyack, *Mar. Ecol.: Prog. Ser.*, 2006, **309**, 279–295.
- 40 B. K. Branstetter, J. S. Trickey and J. J. Finneran, *Eff. Noise Aquat. Life*, 2012, **730**, 29–31.
- 41 P. E. Sitorus, Y. Y. Nazaruddin, E. Leksono and A. Budiyo, *J. Bionic Eng.*, 2009, **6**, 37–45.
- 42 X. Gong, K. Yang, J. Xie, Y. Wang, P. Kulkarni, A. S. Hobbs and A. D. Mazzeo, *Adv. Mater.*, 2016, **28**, 7533–7538.
- 43 F. M. Smith and R. P. Croll, *Auton. Neurosci. Basic Clin.*, 2011, **165**, 140–148.
- 44 T. R. Cook, A. Kato, H. Tanaka, Y. Ropert-Coudert and C. A. Bost, *PLoS One*, 2010, **5**, e9839.
- 45 W. Wang, N. G. Kim, H. Rodrigue and S. H. Ahn, *Mater. Horiz.*, 2017, **4**, 367–376.
- 46 H. Rodrigue, W. Wang, D. R. Kim and S. H. Ahn, *Compos. Struct.*, 2017, **176**, 398–406.
- 47 W. Wang, C. Y. Yu, P. A. Abrego Serrano and S. H. Ahn, *Soft Robot.*, 2020, **7**, 283–291.
- 48 W. Wang, H. Rodrigue, H. Il Kim, M. W. Han and S. H. Ahn, *Composites, Part B*, 2016, **98**, 397–405.